Article:
Marchant, Robert and Cuni Sanchez, Aida (2019) Sensitivity of a tropical montane cloud forest to climate change, present, past and future: Mt. Marsabit, N. Kenya. Quaternary Science Reviews. pp. 34-48. ISSN: 0277-3791

https://doi.org/10.1016/j.quascirev.2019.06.016

Supplementary Information: Sensitivity of a montane cloud forest to climate change, present, past and future: Mt. Marsabit, N. Kenya

Sietse O. Los[a], F. Alayne Street-Perrott[a], Neil J. Loader[a], Cynthia A. Froyd[b], Aida Cuní-Sanchez[c], Robert A. Marchant[c]

[a]*Department of Geography, Swansea University, Singleton Park, Swansea SA2 8PP, United Kingdom*
[b]*Department of Biosciences, Swansea University, Singleton Park, Swansea SA2 8PP, United Kingdom*
[c]*York Institute for Tropical Ecosystems, Environment Department, University of York, Heslington, York, YO10 5NG, UK*

Abstract

In the Supplementary Information we provide further details of (1) the processing and correction of Advanced Very High Resolution Radiometer (AVHRR) and MODerate-resolution Imaging Spectroradiometer (MODIS) Normalized Difference Vegetation Index (NDVI) data introduced in Section 2.2 (Article), (2) an analysis of potential errors in the total annual precipitation estimates (Section 2.3.2, Article), (3) details on the local and regional regression models used to estimate the sensitivity of forest extent to climate change (Section 3.4, Article), and (4) the results of the regional regression sensitivity analysis (compare with Fig. 9, Section 3.4; Article).

S1. Processing and correcting AVHRR and MODIS NDVI Data

NDVI data are frequently used to obtain information about spatial and temporal variations in the amount and vigour of vegetation to support ecological, biogeochemical and hydrological studies (Pettorelli, 2013). NDVI is derived from red and near-infrared radiation reflected by the land surface that is measured by a satellite sensor: NDVI = $(\rho_2 - \rho_1)/(\rho_2 + \rho_1)$ with ρ_1 being the red reflectance and ρ_2 the near-infrared reflectance (Tucker, 1979). Healthy vegetation has unique spectral properties; it reflects solar radiation in near-infrared wavelengths and absorbs radiation in red wavelengths. A large difference between near-infrared and red reflectance indicates the presence of dense green vegetation, other land surfaces tend to reflect near-infrared and red radiation in near-equal amounts which results in a NDVI close to zero.

Fourier Adjusted, Solar and sensor zenith angle corrected, Interpolated and Reconstructed (FASIR) Advanced Very High Resolution Radiometer (AVHRR) NDVI data (8 km resolution, monthly time step, 1982–1999) are derived from Pathfinder AVHRR Land data (James and Kalluri, 1994) and are corrected for the effects of sensor degradation and intercalibration differences in successive AVHRRs using invariant desert targets (Los, 1993, 1998), viewing-angle and illumination-angle effects in the NDVI (Los et al., 2005), and atmospheric scattering and absorption by stratospheric aerosols (Los et al., 2000; Vermote et al., 2001). Outliers are removed and missing data filled in using Fourier series (Sellers et al., 1996). The residual error in FASIR-NDVI at its maximum is about 0.05 NDVI (Los et al., 2000). To obtain NDVI data for the summit of Mt Marsabit, the greenest region in its wide surroundings, we selected the maximum NDVI of a 3 by 3 pixel maximum filter; this avoids low NDVI values as a result of geo-location errors

which can be in the order of 1 pixel. Moderate-resolution imaging spectroradiometer (MODIS) Terra 1 km and 250 m 16-day normalised difference vegetation index (NDVI) data (2001–2015) for Mt Marsabit and its surroundings are obtained from the United States Geological Survey (USGS) Land Processes Distributed Active Archive Center (LPDAAC; https://lpdaac.usgs.gov). These data are filtered and interpolated to a monthly time step using the Fourier Adjustment. To integrate MODIS data for the summit with AVHRR NDVI data, anomalies are calculated for the monthly means of the first 8 years of MODIS data and of the last 8 years of AVHRR data. Anomalies of MODIS data are scaled using the ratio of the standard deviation of the last 8 years of AVHRR anomaly data and of the first 8 years of MODIS data; scaled MODIS anomalies are added to the mean monthly values of the last 8 years of AVHRR data; these data are used in Sections 3.1 and 3.2 (Article). For the analyses in Sections 3.3 and 3.4 (Article) and Section S6, which explore associations between NDVI, precipitation and cloud-base height for the Marsabit region, we use entire MODIS scenes from 2000–2015; only the Fourier Adjustment is applied to these MODIS data.

S2. Error analysis of estimates of total and occult precipitation

We consider four alternative explanations for our estimate of occult precipitation on Mt Marsabit (the magnitude of their associated errors is summarised in Table 1, Supplementary Information): (1) the rainfall measurements at the Marsabit weather station are not representative of rainfall measurements in the forest, (2) the AVHRR NDVI data are not representative of the forest, (3) fog occurrence decreases evapotranspiration, which leads to overestimates of occult precipitation, and (4) fog occurrence increases the proportion of diffuse light which leads to higher photosynthetic rates, higher carbon allocation to leaves and higher NDVI values, effectively changing the relationship between NDVI and precipitation. These combined effects need to be in the order of 900 mm per year to explain the excessive greenness of 0.35 NDVI of the forest.

S2.1. Representativeness of rainfall measured at Marsabit

Rainfall measurements from the Marsabit weather station may not be representative of rainfall in the forest for a number of reasons. Because of the high windspeeds the raingauge may catch only a proportion of rainfall or rainfall may be higher in the forest (above 1500 m a.s.l.). than at the raingauge (1345 m a.s.l.) because of the difference in altitude.

Wind-induced undercatch of rainfall. The average wind speed at Marsabit is 8 ±3 m s^{-1}. We do not have detailed information about the raingauge on Mt Marsabit which hampers estimation of the undercatch; the calculation below therefore serves as an illustration. Wind speed measured at 10 m is adjusted to the height of the rain gauge (Yang et al., 1998); for the purpose of comparison here assumed to be 1 m above the surface:

$$U(h) = U(H)\ln(h/z0)/\ln(H/z0) \quad \text{(S1)}$$

with $U(h)$ the estimated daily wind speed (m s^{-1}) at the opening of the gauge; $U(H)$ the measured daily wind speed at 10 m (m s^{-1}), h and H are the heights (m) of the gauge and anemometer, respectively and z_0 is the surface roughness (m). Undercatch for a raingauge with a 20 cm diameter opening is approximated by:

$$R_s = \exp(4.606 - 0.041U(h)^{0.69}) \quad \text{(S2)}$$

$$R_u = \exp(4.605 - 0.062U(h)^{0.58}). \quad \text{(S3)}$$

with R_s being the catch ratio for a shielded gauge and R_u the catch ratio for an unshielded gauge (Yang et al., 1998).

The above correction was developed for rain gauges in Alaska using the World Meteorological Organization (WMO) recommended method for measuring undercatch; the above equations were derived for a wide range of conditions in terms of wind speed, temperature, rain intensity and droplet size (Yang et al., 1998). The correction was found to improve measurement accuracy for other areas and climates as well (Sieck et al., 2007).

From average daily wind speeds at Mt Marsabit, we find an average undercatch of 75 mm y^{-1} for an unshielded raingauge and an average undercatch of 81 mm y^{-1} for a shielded raingauge; the undercatch is similar in magnitude to that found elsewhere (Yang et al., 1998; Sieck et al., 2007) and is larger than a correction of 2% applied to global data (Adam and Lettenmaier, 2003). The estimated undercatch is an order of magnitude smaller than our estimate of occult precipitation and is therefore not an alternative explanation for the excessive greenness of Mt Marsabit. It is important to note that no correction was incorporated in the processing stream of the CRU data for wind effects (Harris et al., 2014), since it is unlikely that the station data used to assemble the CRU precipitation data were corrected for undercatch. By not implementing a correction for undercatch we compare like with like, i.e. uncorrected rainfall data at the Marsabit weather station with uncorrected CRU data for the tropics.

Orographic effect on rainfall. The orographic effect is estimated using the CRU data for the larger Marsabit region (latitude 1 °S–8 °N; longitude 35–42 °E). A regression with the mean annual precipitation data for 1973–2013 as dependent variable and elevation from the 0.5 degree hydro1k data finds a mean orographic effect of 0.44 mm m^{-1} (± 0.2 mm m^{-1}). The elevation of the top of Mt Marsabit is 1707 m a.s.l. The maximum height in the Space shuttle Radar Topography Mission (SRTM) data, which have a spatial resolution of 90 m, is 1689 m a.s.l. The maximum average height for an area the size of a Glbal Area Coverage (GAC) AVHRR pixel (4.4 by 1.1 km) is 1509 m a.s.l. The elevation difference between the maximum average height of a GAC pixel (1509 m a.s.l.) and Marsabit weather station (1345 m a.s.l.) is 164 m, hence the mean orographic effect is about 73 mm which we added to measurements of annual precipitation to adjust for its effect. A similar analysis of station data in the region (not shown) showed a smaller orographic effect.

Comparison Marsabit rainfall with forest data. Rainfall for 3 rainy seasons between October 2014 and December 2015 measured at the Marsabit weather station (1120 mm) and at the lodge by AC-S (1140 mm) only differed by a small amount. The partial correlations between rainfall at Marsabit station and NDVI did not decline with distance. We therefore conclude that rainfall measured at Marsabit is representative of the forest and that rainfall variability at the station is representative of rainfall variability for the wider region.

S3. Representativeness of AVHRR NDVI data

AVHRR NDVI data are coarse-resolution data (1.1 by 4.4 km AVHRR Global Area Coverage (GAC) data — 4.84 km^2) that are navigated to an 8 km (64 km^2) resolution with an error smaller than 4 km latitude and 8 km longitude (James and Kalluri, 1994; Young and Anyamba, 1999); the forest area is approximately 120 km^2. We selected the maximum NDVI of a 3×3 pixel window to obtain a best estimate of forest greenness since the summit of Mt Marsabit is the greenest area in the region. Selection of a pixel further away from the summit would result in selecting a

lower NDVI value, which would lower our estimate of total precipitation. Other errors in NDVI reduce its value as well (Holben, 1986; Los et al., 1994); hence the NDVI can underestimate the amount of occult precipitation but is unlikely to overestimate it. The residual error in AVHRR NDVI data, after a range of corrections have been applied (Los, 1993, 1998; Los et al., 2000, 2005; Sellers et al., 1996; James and Kalluri, 1994; Vermote et al., 2001), is around 0.05 NDVI (Los et al., 2001) which is equivalent to 135 mm precipitation. This is 6 times smaller than our estimate of occult precipitation and is incorporated in the overall uncertainty of our method (±265 mm).

The NDVI climatology for April, the month of highest rainfall and highest occurrence of fog, shows a lower value than that of the preceding month. In most of the tropics the response in NDVI lags the occurrence of precpitation by 2–4 weeks, in line with the 1-month lag in occult precipitation and 0-month lag with rainfall (Fig. 2 and 8; Article). In the unlikely case that the depressed April NDVI value is caused by sub-pixel cloud contamination, we can estimate its maximum effect on the estimation of occult precipitation as follows. We assume the correct value for April is the highest value of the time series, i.e. we replace 0.68 with 0.72. This will increase the mean annual NDVI by 0.0034 and our annual estimate of occult precipitation by 11 mm. This error is an order of magnitude smaller than the uncertainty of the method and is therefore ignored in our estimates of occult precipitation.

S4. Effect of fog on evapotranspiration

Evapotranspiration is reduced during fog because of lower down-welling solar radiation, lower surface air temperatures and increased atmospheric humidity. We estimate this reduction using data from 1985–1998. This period shows the highest agreement between the number of annual fog days obtained from the Kenya Meteorological Service (KMS) and the number of annual fog days calculated from the Marsabit ISD record held at NOAA. A fog day is identified from the ISD log (under field AY1 or AY2), or from visibility values lower than 900 m. The coefficient of correlation between the ISD and KMS number of fog days per year is 0.94, the root-mean-square error is 16 days per year and the bias 2.2 days per year (KMS has higher values). We use the Makkink and Priestley-Taylor methods to estimate potential evapotranspiration (McMahon et al., 2013). The Penman-Monteith equation is deemed less desirable for our case because its use can result in large errors when it is not properly calibrated to local conditions (De Bruin, 1987; De Bruin et al., 2010). Average wind speed under fog conditions is 9.0 m s^{-1} and under non-fog conditions 9.2 m s^{-1}; this results in a very small difference in evapotranspiration when a dependency of evapotranspiration on wind speed is considered as per the Penman-Monteith equation.

Temperature, humidity and cloudiness data are obtained from the NOAA ISD Marsabit data; net shortwave radiation is estimated from cloud cover and latitude (McMahon et al., 2013). For the Priestley-Taylor method the ground heat flux is set to zero and albedo is set to 0.16. Daily potential evapotranspiration rates are calculated for 1985–1998. The evapotranspiration is averaged both for each fog and each fog-free Julian day between 1985–1998, resulting in a 1-year fog-free and a 1-year fog climatology. There are three fog-free Julian days missing in 1985–1988 (days 109, 118 and 332); evapotranspiration rates for these three days is estimated by linear interpolation of values from the previous and subsequent days. Annual potential evapotranspiration for the fog-free year is between 1213 mm (Makkink) and 1724 mm (Priestley-Taylor) and for the fog year between 918 mm (Makkink) and 1395 mm (Priestley-Taylor). We estimate a reduction in potential evapotranspiration of 0.8 mm per fog day using the Makkink method and of 0.9 mm

per fog day using the Priestley Taylor method. This translates to a maximum overestimate of occult precipitation between 160–180 mm per year for the 1980s (about 200 fog days) and between 80–90 mm per year after 2000 (about 100 fog days). There is uncertainty in estimating the reduction of actual evapotranspiration during fog, e.g. in a recent study in a montane forest in Taiwan it was found that actual evapotranspiration increased during fog by about 0.2 mm per day (Beiderwieden et al., 2008). We conclude that the effect of fog on evapotranspiration is too small to be an alternative explanation for our estimate of occult precipitation.

S5. Effect of fog on gross primary productivity (GPP) and NDVI

Fog affects plant photosynthesis in a number of ways: it increases the proportion of diffuse radiation which stimulates GPP; but it also reduces the total amount of solar radiation which reduces GPP (Alton et al., 2007). Fog also affects photosynthesis since it increases atmospheric humidity and decreases air temperatures. Similar to section S4 (above), we calculate a climatology of cloud cover, temperature and humidity for a non-fog year and a fog year by taking the average values for non-fog days and fog days for each Julian day from 1985–1998. Down-welling radiation is calculated from cloud cover, surface air temperature, relative humidity, time of year and latitude (McMahon et al., 2013). The diffuse and direct fraction of down-welling solar radiation is estimated using Paltridge and Platt (1976):

$$\begin{aligned} f_d &= R_d/(R_b + R_d) \\ R_d &= (0.00913 + 0.0125(90 - \theta) + 0.723 * C_o)\cos\theta \\ R_b &= 3.42286[1 - \exp(-0.075(90 - \theta))], \end{aligned} \tag{S4}$$

with R_d and R_b being the diffuse radiation and direct radiation respectively, f_d the diffuse fraction, θ the solar zenith angle (in degrees) and C_o the cloud octa. We use the model of Roderick et al. (2001) to calculate annual gross primary productivity:

$$\begin{aligned} P'_G &= e' f'_{\mathrm{APAR}} C' R'_s \\ e' &\approx 0.024 + 0.11 R_d/R_s - 0.018(R_d/R_s)^2 \end{aligned} \tag{S5}$$

with P'_G being the annual gross primary productivity (mol CO_2 m^{-2} y^{-1}); e' the efficiency of the canopy (mol CO_2 mol^{-1} photosynthetically active radiation — PAR), and f_{APAR} the fraction of photosynthetically active radiation (here 0.95 to obtain a maximum estimate), R_d the diffuse radiation calculated as above, and $C = 2.3$ mol PAR MJ^{-1} converting the global solar irradiance R_s (M J y^{-1}) to quanta in the PAR region.

For 365 fog days we estimate a 15% to 19 % lower GPP than for non-fog days; this indicates that annual GPP during fog days is reduced by 8% to 10 % in the early 1980s (200 fog days per year) and by 4% to 5% after 2000 (100 fog days per year). A change in annual GPP is proportional to a change in the mean annual fraction of photosynthetically active radiation intercepted by the vegetation canopy (Monteith, 1972; Monteith and Moss, 1977; Potter et al., 1993) and is near-linearly related to the mean annual NDVI (Tucker and Sellers, 1986; Myneni et al., 1995). Therefore, we approximate the error of fog occurrence on annual precipitation from the linear relationship between NDVI and annual precipitation (Fig. 5 Article). Since we underestimate GPP, and hence NDVI, on Mt Marsabit, we need to add 200 mm to our estimates of occult precipitation during the 1980s (about 10 % of NDVI) and 100 mm after 2000 (about 5% of NDVI). Because

the estimate of the effect of diffuse radiation on NDVI is opposite in sign and of equal magnitude to the effect of fog on evapotranspiration, we ignore both factors. This results in a residual uncertainty equivalent to about 20 mm precipitation per year which is an order of magnitude smaller than the uncertainty in the relationship shown in Fig. 5 (Article).

Table S1: Error estimates for occult precipitation related to undercatch of rain because of wind effects, the effects of fog, orographic effects and systematic errors in NDVI caused by residual clouds. Fog on Mt Marsabit reduces both evapotranspiration and photosynthesis (Gross Primary Productivity — GPP), which potentially affects the NDVI and the estimate of total precipitation derived from it. Effects of fog on evapotranspiration and photosynthesis are of opposite sign and similar in magnitude and are therefore ignored. Numbers under "PPN (Precipitation) equivalent" and "Correction" need to be added to estimates of occult precipitation. Orographic effect, E_O, is added to annual rainfall as a positive number (see eq. 3, Article).

	Estimate	PPN equivalent	Correction
Undercatch	12%	-80 mm	0
Evapotranspiration	80–180 mm	-80 – -180 mm	0
GPP	-20 %	+100 – +200 mm	0
Orographic effect	40 mm / 100 m	-73 mm	-73 mm
Cloud contamination (April)	0.0034	+11 mm	0

S6. Estimation of climate change sensitivity

We used two models to study the sensitivity of forest extent on Mt Marsabit to changes in cloud-base height, rainfall and atmospheric humidity; one is a local regression model and the other a regional regression model

Local regression model. For the local regression model, monthly NDVI is estimated per 250 m×250 m pixel from monthly rainfall (zero lag) and monthly cloud-base height (leading NDVI by 1 month) using:

$$V_{i,j} = \beta_{0,i,j} + \beta_{1,i,j} P_R + \beta_{2,i,j} z_C, \tag{S6}$$

with $V_{i,j}$ being the monthly NDVI for pixel with coordinate i, j, $\beta_{0,i,j}$ and $\beta_{1,i,j}$ the regression coefficients for coordinate i, j; P_R the monthly rainfall measured at Mt Marsabit, and z_C the mean monthly cloud-base height calculated from Mt Marsabit temperature and dew-point temperature data with eq. 1 (Article). Missing precipitation and cloud-base height data (data missing for 3 months) are replaced with climatological averages. Equation 1 (Article) allows calculation of the sensitivity of cloud-base height to a change in surface air temperature. Coefficients for equation S6 are estimated using canonical correlation to avoid reducing the variance in the dependent variable $V_{i,j}$ (Draper and Smith, 1998). The amount of variance explained by the local regression model (using 401×401 equations) is 86 %.

Regional regression model. For this model, NDVI is estimated from rainfall, cloud-base height, location and altitude using one equation for the entire region. Coefficients are estimated using

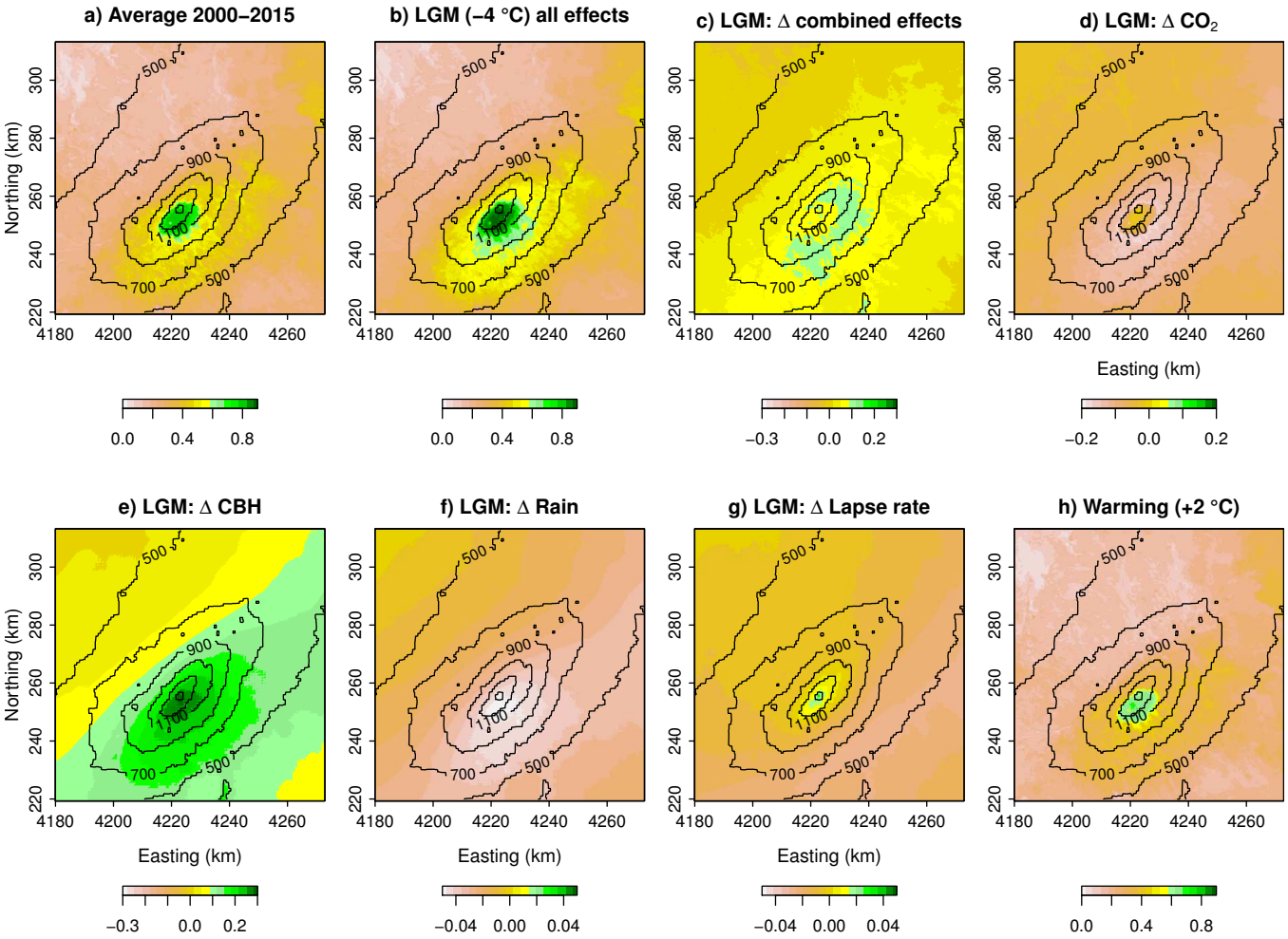

Figure S1: a. Average NDVI of the Marsabit region for 2000–2015; NDVI = 0.7 coincides with the lower boundary of the xeromorphic forest. b. Projected NDVI for the LGM. c. Change in LGM NDVI compared to current conditions (b. - c.). d. Reduction in LGM NDVI resulting from lower atmospheric CO_2 concentrations e. Change in LGM NDVI caused by a 500 m lower cloud-base height. f. Change in LGM NDVI as a result of 30 % lower rainfall. g. Change in LGM NDVI caused by a change in lapse rate (Loomis et al., 2017). h. Projected NDVI as a result of a 250 m increase in cloud-base height caused by 2 °C warming. (Sinusoidal projection; Easting — distance from the Greenwich meridian; Northing — distance from equator.) See Fig. 9 (Article) for comparison.

canonical correlation:

$$
\begin{aligned}
V \quad = \quad & \beta_0 + \beta_1 P_R + \beta_2 P_R x + \beta_3 P_R y + \beta_4 P_R xy + \\
& \beta_5 z_C + \beta_6 z_C x + \beta_7 z_C y + \beta_8 z_C xy + \\
& \beta_9 h + \beta_{10} hx + \beta_{11} hy + \beta_{12} hxy + \\
& \beta_{13} hP_R + \beta_{14} hP_R x + \beta_{15} hP_R y + \beta_{16} hP_R xy + \\
& \beta_{17} hz_C + \beta_{18} hz_C x + \beta_{19} hz_C y + \beta_{20} hz_C xy + \\
& \beta_{21} x + \beta_{22} y + \beta_{23} xy,
\end{aligned}
\tag{S7}
$$

with V being a three dimensional array (401 by 401 pixels of 250 m×250 m and 180 months) of NDVI data from 2000–2015, and P_R an array of the same size as V filled with monthly rainfall data at zero lag with the NDVI observation ($t = 0$), z_C an array with cloud-base height data from the Mt Marsabit station for the month leading the NDVI data; x, y and h arrays of the same dimensions as V filled with the x-coordinate, the y-coordinate and elevation, respectively. Spatial variation in rainfall and variation in rainfall with elevation are taken into account by the interaction terms $P_R x$, $P_R y$, $P_R h$, $P_R xy$, $P_R hx$, $P_R hy$ and $P_R hxy$ and spatial and height dependencies in cloud-base height by the interaction terms $z_C x$, $z_C y$, $z_C h$, $z_C xy$, $z_C hx$, $z_C hy$ and $z_C hxy$. Spatial and height interactions are also accounted for by the terms hx, hy and hxy. In contrast to the first method (eq. S6), the regression coefficients $\beta_0 \ldots \beta_{23}$ pertain to the entire 401 by 401 pixels by 180 months array and have no spatial variability. An analysis of variance (ANOVA) on the same model but using ordinary least squares shows that all independent variables are significant ($p << 0.05$) and that their combined amount of variance explained is 63 %.

S6.1. NDVI sensitivity analysis from global regression

The regional regression model is used to estimate the sensitivity of NDVI to changes similar to the sensitivity analysis shown for the local regression model. There is no particular good reason to prefer one model over the other, the regional model is expected to be more sensitive in areas with high and low NDVI whereas the local model provides a closer match to observations. The models are used to obtain an estimate of uncertainty in the extrapolation of the model to the LGM and to the global warming scenario. Cloud-base height is reduced by 500 m, rainfall by 30 %, NDVI by 20 % as a result of reduced atmospheric CO_2 concentrations, and the lapse rate is adjusted using data from Loomis et al. (2017). Results are shown in Fig. S1, see Fig. 9 (Article) for comparison. Changes in surface area with NDVI above 0.6, 0.7 and 0.8 are shown in Table 3 (Article).

Bibliography

Adam, J. C., Lettenmaier, D. P., 2003. Adjustment of global gridded precipitation for systematic bias. J. Geophys. Res. 108, 4257, doi:10.1029/2002JD002499.

Alton, P. B., North, P. R. J., Los, S. O., 2007. The impact of diffuse sunlight on canopy light-use efficiency, gross photosynthetic product and net ecosystem exchange in three forest biomes. Glob. Change Biol. 13, 776–787, doi: 10.1111/j.1365–2486.2007.01316.x.

Beiderwieden, V. W., Hsia, Y. J., Klemm, O., 2008. It goes both ways: measurements of simultaneous evapotranspiration and fog droplet deposition at a montane cloud forest. Hydrol. Process. 15, 4182–4189, doi: 10.1002/hyp.7017.

De Bruin, H. A. R., 1987. From Penman to Makkink. Tech. rep., TNO publ. Evaporation and Weather, The Hague, The Netherlands.

De Bruin, H. A. R., Trigo, I. F., Jitan, M. A., Temesgen Enku, N., Van der Tol, C., Gieske, A. S. M., 2010. Reference crop evapotranspiration derived from geo-stationary satellite imagery: a case study for the Fogera flood plain, NW-Ethiopia and the Jordan Valley, Jordan. Hydrol. Earth Syst. Sc. 14, 2219–2228, doi: 10.5194/hess–14–2219–2010.

Draper, N. E., Smith, H., 1998. Applied Regression Analysis, 3rd Edition. John Wiley, Hoboken, New Jersey.

Harris, I., Jones, P. D., Osborn, T. J., Lister, D. H., 2014. Updated high-resolution grids of monthly climatic observations – the CRU TS3.10 dataset. Int. J. Climatology 34, 623–712, doi: 10.1002/joc.3711.

Holben, B. N., 1986. Characteristics of maximum-value composite images from temporal AVHRR data. Int. J. Remote Sens. 7, 1417–1434.

James, M. E., Kalluri, S. N. V., 1994. The Pathfinder AVHRR Land data set - an improved coarse resolution data set for terrestrial monitoring. Int. J. Remote Sens. 15 (17), 3347–3363.

Loomis, S., Russell, J., Verschuren, D., Morrill, C., De Cort, G., Sinninghe Damsté, J., Olago, D., Eggermont, H., Street-Perrott, F., Kelly, M., 2017. The tropical lapse rate steepened during the last glacial maximum. Science Advances 3, e1600815, doi: 10.1126/sciadv.1600815.

Los, S. O., 1993. Calibration adjustment of the NOAA Advanced Very High Resolution Radiometer without recourse to component channel-1 and channel-2 data. Int. J. Remote Sens. 14, 1907–1917.

Los, S. O., 1998. Estimation of the ratio of sensor degradation between NOAA AVHRR channels 1 and 2 from monthly NDVI composites. IEEE T. Geosci. Remote 36, 206–213, doi: 10.1109/36.655330.

Los, S. O., Collatz, G. J., Bounoua, L., Sellers, P. J., Tucker, C. J., 2001. Global interannual variations in sea surface temperature and land surface vegetation, air temperature, and precipitation. J. Climate 14, 1535–1549.

Los, S. O., Collatz, G. J., Sellers, P. J., Malmstrom, C. M., Pollack, N. H., DeFries, R. S., Bounoua, L., Parris, M. T., Tucker, C. J., Dazlich, D. A., 2000. A global 9-yr biophysical land surface dataset from NOAA AVHRR data. J. Hydrometeorology 1, 183–199.

Los, S. O., Justice, C. O., Tucker, C. J., 1994. A global 1-degrees-by-1-degrees NDVI data set for climate studies derived from the GIMMS continental NDVI data. Int. J. Remote Sens. 15, 3493–3518.

Los, S. O., North, P. R. J., Grey, W. M. F., Barnsley, M. J., 2005. A method to convert AVHRR normalized difference vegetation index time series to a standard viewing and illumination geometry. Remote Sens. Environ. 99, 400–411, doi: 10.1016/j.rse.2005.08.017.

McMahon, T. A., Peel, M. C., Lowe, L., Srikanthan, R., McVicar, T. R., 2013. Estimating actual, potential, reference crop and pan evaporation using standard meteorological data: A pragmatic synthesis. Hydrol. Earth Syst. Sc. 17, 1331–1363, doi: 10.5194/hess–17–1331–2013.

Monteith, J. L., 1972. Solar radiation and productivity in tropical ecosystems. J. Appl. Ecol. 9, 747–766.

Monteith, J. L., Moss, C. J., 1977. Climate and the efficiency of crop production in britain. Philos. T. Roy. Soc. B 281, 277–294.

Myneni, R. B., Hall, F. G., Sellers, P. J., Marshak, A. L., 1995. The interpretation of specral vegetation indexes. IEEE T. Geosci. Remote 33, 481–486.

Paltridge, C. W., Platt, C. M. R., 1976. Radiative Processes in Meteorology and Climatology. Elsevier, Amsterdam.

Pettorelli, N., 2013. The Normalized Difference Vegetation Index. Oxford University Press, Oxford, United Kingdom, 208 pp.

Potter, C. S., Randerson, J. T., Field, C. B., Matson, P. A., Vitousek, P. M., Mooney, H. A., Klooster, S. A., 1993. Terrestrial ecosystem production: A process model based on global satellite and surface data. Global Biogeochem. Cy. 7, 811–841.

Roderick, M. L., Farquhar, G. D., Berry, S. L., Noble, I. R., 2001. On the direct effect of clouds and atmospheric particles on the productivity and structure of vegetation. Oecologia 129, 21–30, doi: 10.1007/s004420100760.

Sellers, P. J., Los, S. O., Tucker, C. J., Justice, C. O., Dazlich, D. A., Collatz, G. J., Randall, D. A., 1996. A revised land-surface parameterization (SiB2) for atmospheric GCMs. part 2: The generation of global fields of terrestrial biophysical parameters from satellite data. J. Climate 9, 706–737.

Sieck, L. C., Burges, S. J., Steiner, M., 2007. Challenges in obtaining reliable measurements of point rainfall. Water Resour. Res. 43, W01420, doi: 10.1029/2005WR004519, Correction Published 20 June 2007.

Tucker, C. J., 1979. Red and photographic infrared linear combinations for monitoring vegetation. Remote Sens. Environ. 8, 127–150.

Tucker, C. J., Sellers, P. J., 1986. Satellite remote sensing of primary production. Int. J. Remote Sens. 7, 1395–1416.

Vermote, E. F., Justice, C. O., Descloitres, J., El Saleous, N., Roy, D. P., Ray, J., Margerin, B., Gonzalez, L., 2001. A SeaWiFS global monthly coarse-resolution reflectance dataset. Int. J. Remote Sens. 22, 1151–1158.

Yang, D., Goodison, B. E., Ishida, S., Benson, C. S., 1998. Adjustment of daily precipitation data at 10 climate stations in Alaska: Application of World Meteorological Organization intercomparison results. Water Resour. Res. 34, 241–256, doi: 10.1029/97WR02681.

Young, S., Anyamba, A., 1999. Comparison of NOAA/NASA PAL data for vegetation change studies over China. Photogramm. Eng. Rem. S. 65, 679–688.